

A Numerical Framework for Multiparametric Optimization of Distributed Electric Propulsion

Original

A Numerical Framework for Multiparametric Optimization of Distributed Electric Propulsion / Comunian, P., Serpieri, J., Cafiero, G.. - In: JOURNAL OF AIRCRAFT. - ISSN 0021-8669. - (2025), pp. 1-11. [10.2514/1.c038541]

Availability:

This version is available at: 11583/3006269 since: 2026-01-15T15:43:14Z

Publisher:

American Institute of Aeronautics and Astronautics, AIAA

Published

DOI:10.2514/1.c038541

Terms of use:

This article is made available under terms and conditions as specified in the corresponding bibliographic description in the repository

Publisher copyright

AIAA preprint/submitted version e/o postprint/Author's Accepted Manuscript

(Article begins on next page)

A numerical framework for multi-parametric optimization of distributed electric propulsion*

Paolo Comunian [†], Jacopo Serpieri [‡] and Gioacchino Cafiero [§]
*Department of Mechanical and Aerospace Engineering,
Politecnico di Torino, Corso Duca degli Abruzzi 24, Turin, Italy, 10129*

We investigate the interaction of tractor propellers in a distributed propulsion configuration with a lifting surface. An optimization framework is constructed based on genetic algorithms. An aero-propulsive model for propeller-wing systems in a tractor configuration is developed based on a vortex lattice method lifting-line for the aerodynamic lifting surfaces, coupled with a blade element momentum theory model to describe the propellers. We define the optimum based on different figures of merit, namely the lift, the propulsive efficiency, and the aerodynamic efficiency. Configurations with a number of propellers ranging from 2 to 12 are explored, showing that a 10% increase in lifting capabilities is achievable with the use of distributed propulsion on a wing representative of a regional transport aircraft. By using a data-driven optimization scheme, a quick assessment of a vast number of conditions becomes possible, enabling to tackle the problem from a multi-objective optimization point of view. This opens a discussion that is not necessarily centered on the value of the optimized metric, but on the combination of parameters and physical relations that constitute an optimized case. We conclude by extending the numerical model into a panel code to assess the implications of distributed propulsion on the horizontal tail of an aircraft.

Nomenclature

Symbols

C_L	=	lift coefficient
C_D	=	drag coefficient
E	=	aerodynamic efficiency
T	=	thrust [N]
Q	=	torque [Nm]

*Part of this work was presented at the AIAA Aviation Forum 2024 - AIAA 2024-3603 - 10.2514/6.2024-3603

[†]Corresponding author, Ph.D student, paolo.comunian@polito.it.

[‡]Assistant professor, jacopo.serpieri@polito.it.

[§]Associate professor, gioacchino.cafiero@polito.it

T_c	=	thrust coefficient	$T / \left(\frac{1}{2} \rho V_\infty^2 \pi R^2 \right)$
Q_c	=	torque coefficient	$Q / \left(\frac{1}{2} \rho V_\infty^2 \pi R^3 \right)$
η	=	efficiency	
V	=	velocity	[m/s]
J	=	advance ratio	$V / (nD)$
N_p	=	number of propellers	
R	=	radius	[m]
n	=	rotational frequency	[1/s]
b	=	wing span	[m]
c	=	chord	[m]
AR	=	aspect ratio	
α	=	angle of attack	
β	=	blade pitch angle	
ρ	=	Pearson correlation coefficient	
WF	=	washed fraction	
$eqDL$	=	equivalent disk loading	
Δ	=	variation	
$err_{\chi, \%}$	=	relative percentage error on χ	

Abbreviations

DEP	=	distributed electric propulsion
VLM	=	vortex lattice method
LBM	=	lattice Boltzmann method
RANS	=	Reynolds-averaged Navier-Stokes
VPM	=	vortex particle method
FVW	=	free vortex wake
STM	=	stream tube model
BEMT	=	blade element momentum theory
DBS	=	down-going blade side
UBS	=	up-going blade side
MDS	=	multidimensional scaling

Subscripts

p	=	propeller
-----	---	-----------

iw = isolated wing
inn = inner
out = outer

I. Introduction

DISTRIBUTED electric propulsion (DEP) aircraft concepts have gained attention due to them being suitable candidates for electrification, contributing to the reduction of direct CO_2 emissions [1]. For the last fifty years, turbofans have been the standard for aircraft propulsion, with this sector nowadays pushing towards larger engines [2]. Meanwhile, sustainable aviation fuels (SAF) [3] are also being tested to mitigate the environmental impact of aviation [4, 5].

Propellers have been widely adopted for DEP as the interaction between the propeller’s slipstream and the wing in a tractor configuration has been shown to bring an increase in lifting capabilities [6] and aerodynamic efficiency [7], opening the possibility for battery or fuel-cell powered aircraft. This is achieved by leveraging the aero-propulsive coupling between the propulsion system and the lifting surfaces [8, 9]. Examples of this are NASA’s X-57 program [10] or the Electra EL-2 Goldfinch [11] aircraft. However, hybrid-electric or fully electric architectures are generally associated with a higher overall weight [12], mainly due to the energy storage, such as batteries or hydrogen reservoirs [13]. These kinds of aircraft are unlikely to achieve ranges similar to those of long-range, wide-body airliners in the near future [14, 15], in particular at the same maximum take-off weight.

Nevertheless, future technological developments are expected to make DEP a viable solution. The effectiveness of a DEP architecture depends on multiple interlinked factors [12, 16], ranging from the power-to-weight ratio of the various components, the propeller’s position, or the blade’s geometry.

The complexity and the multidimensionality of the problem can benefit from a holistic approach that allows for the concurrent consideration of multiple factors. We present an optimization framework based on genetic algorithms to search for optimal DEP configurations that improve lift and aerodynamic efficiency. This novel approach is of interest as it can lead to a faster time in defining an optimal condition from the aerodynamic perspective.

Modelling propeller-wing interaction is essential to designing DEP architectures. Several numerical approaches are found in the literature in the context of DEP. High to mid fidelity CFD simulations that capture the full physics of the problem are achieved using the Lattice Boltzmann Method (LBM) [17] or the Reynolds-averaged Navier-Stokes equations (RANS) [8, 18], while mid to low fidelity simulations, albeit with less computational power, use Vortex Particle Method (VPM) [19–21], or Free Vortex Wake (FVW) approaches [22]. However, the computational cost of these approaches makes them unsuitable for multi-parametric (optimization) studies, where many iterations, and thus simulation runs, are needed. Analytical or semi-analytical models allow for a fast computation of the aerodynamic coupling between the wing and the propulsive system [23].

Most examples of fast numerical approaches found in the literature are commonly based on momentum theory, as proposed by Patterson et al. [24]. Applications are found in DEP aircraft concept design [12, 25, 26], design optimization [27], or trajectory optimization [28]. Although numerically inexpensive, this simplified approach neglects the effects of the swirl induced by the propeller and, to some extent of the spanwise location of the propeller, making it impossible to evaluate a proper spanwise load distribution for a wing with propellers, specifically relevant for tractor configurations. In addition, this approach does not consider the characteristics of the propellers in use, but is rather limited to the thrust coefficient, which can be an insufficient parameter from a design perspective.

Within the developed framework, a numerical aero-propulsive model is included, which is capable of estimating the lift and drag distribution over a wing due to the interaction of an array of propellers in tractor configuration. This model is based on the blade element momentum theory (BEMT) method, which was used to estimate the propeller forces, and on the vortex lattice method (VLM) to describe the wing, accounting for the effect of the induced swirl by the propellers; similarly to the work of Naderlof et al. [29].

Leveraging on the developed numerical framework, a study was conducted over different configurations featuring different numbers of propellers for a wing representative of a regional transport aircraft with distributed propulsion. This not only yielded optimal configurations, in terms of propeller's spanwise positioning and operating conditions, leading to a maximum lift augmentation of 10 %, but also allowed to elucidate which characteristics of a DEP configuration based on tractor propellers are associated with the high lift or high aerodynamic efficiency.

Finally, the aerodynamic model was extended to a three-dimensional panel code. This allowed us to assess the implications of the increased lifting capabilities on a secondary lifting surface located downstream the propeller-wing configuration. The paper first discusses, in section II, the numerical framework employed, describing the propeller-wing modelling and the optimization framework, as well as presenting a validation of the model. Sections III and IV present the case study and results of this paper. Finally, section V presents a 3D panel code as an extension of the presented framework. The main conclusions, limitations, and outlooks of this work are discussed in section VI.

II. Numerical framework

A. Propeller-wing modelling

The modelling of the interaction between the propeller and the wing is based on a combination of the VLM formulation of a lifting line and the BEMT (described in detail in appendix A). The implemented BEMT model also allows for asymmetric inflow conditions. As such, the thrust and torque of the propeller can also be estimated considering non-zero angles of attack and sideslip.

The interaction between the wing and the propeller's slipstream is modelled in terms of the wing velocity and angle of attack variation for the wing sections, along the span, washed by the propellers' slipstream, and neglecting any

contraction of the propellers' slipstream. The interaction among propellers is also neglected, as this is only relevant when propellers are at less than a propeller radius distance from each other [30]. Although this interaction is known to cause changes to the performance and the slipstream with respect to an isolated propeller case, this change is rather small, limited to a 1.5% reduction of propulsive efficiency [31]. Finally, also the effect of the wing on the propellers was not included, being a second-order effect with respect to the propeller slipstream effect on the wing. Radial and angular distributions of induced axial and tangential velocities are computed for each propeller using the BEMT model. These values are then translated into the wing's reference frame and summed to the incoming flow velocity, leading to an effective velocity V_{eff} and angle of attack α_{eff} (Figure 1) along the wingspan, which are then used as input for the VLM.

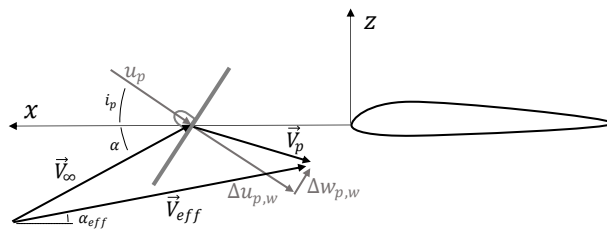


Fig. 1 Effective velocity V_{eff} and angle of attack α_{eff} due to the propeller induced velocity V_p .

The washed area of the wing is schematically indicated as “interaction zone” in Figure 2. This is assumed to be the projection, along the free stream direction, of the propeller onto the wing. This approach does not consider the contraction of the slipstream or its deformation over the wing [32–34], and assumes that the center of the propeller's disk is placed along the chord line. Nederlof et al. [29] included this effect via a stream tube model (STM).

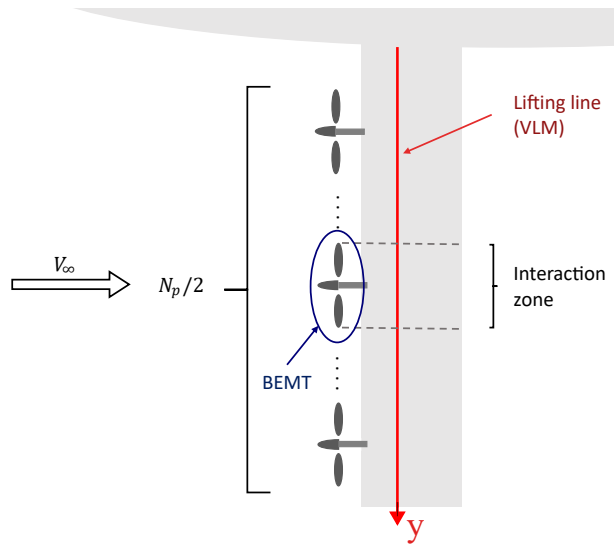


Fig. 2 Schematic representation of the numerical model.

The down-going blade side (DBS) and the up-going blade side (UBS) induce downwash and upwash in the wake,

respectively, as shown in Figure 3. In addition, if the propeller is positioned with a relative angle of attack with respect to V_∞ , the propeller disk will see a non-uniform loading. As a consequence, the induced velocities will be different between the UBS and the DBS.

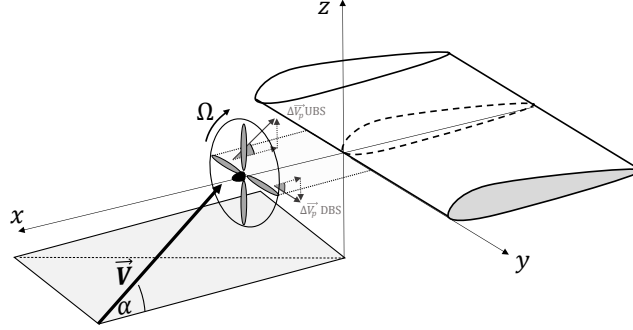


Fig. 3 Schematics of the considered configuration representing a propeller in tractor configuration. The incoming flow velocity and the propeller-induced velocity are shown together with the considered reference frame.

The numerical model allows for the computation of the lift and drag distributions along the wingspan, as well as the induced drag. The drag distribution, consisting of pressure and skin friction drag, is obtained by assuming the local value of the friction drag associated to the wing sections' polars obtained with XFOIL 6.9 [35]. The polars are evaluated for a range of Reynolds numbers and stored in a database, which can be queried once the section lift distribution is known. The induced drag is calculated from the lift distribution using the Trefftz-plane method [36].

The implemented optimization framework considers six variables related to the propeller position, characteristics, and operating conditions. For each one of the N_p propellers, denoted with the subscripts 'i', the variables are the propeller's thrust ($T_{p,i}$), span-wise position ($y_{p,i}$), radius ($R_{p,i}$), rotation direction ($rot_{p,i}$) (inboard-down or inboard-up), pitch relative to the chord line ($i_{p,i}$) and the blade root pitch ($\beta_{p,i}$). The last one represents the fixed blade pitch variation for the entire blade. The blade characteristics, such as the airfoil's geometry, the chord, and the twist radial distributions are fixed and equal for all propellers. Other variables included are the chord (c) and the wingspan (b) of a rectangular wing, the wing's airfoil, the wing's geometric angle of attack (α), the sidewash angle and the inflow velocity (V_∞).

B. Optimization framework

The goal of the current study is to obtain optimized DEP configurations in terms of lift and aerodynamic efficiency enhancement. To this end, only five of the six variables for each propeller were considered. The propeller pitch (i_p) was not included as an optimization variable, as it was found that a negative pitch would always yield an increment in effective angle of attack, and, as a consequence, of the lift coefficient. In addition, an excessively large propeller pitch goes against the hypothesis that the wing is completely immersed in the propeller slipstream. To avoid falling into cases that cannot be properly described by the implemented numerical framework, $i_{p,i}$ was kept equal to zero for all propellers during the optimization, as otherwise the optimization algorithm might find results that are not representative of reality.

Any given configuration is reasonably assumed symmetrical with respect to the wing's centreline, and, as such, just half of the variables are needed. The total thrust is fixed and equal to a fixed predetermined value. In the cases discussed in this work, this was set to the drag assuming a C_D equal to 0.025, representative of the desired optimization condition, which was horizontal flight. In addition, to have a constant total thrust, one of the propeller thrust values ($T_{p,i}$) is determined by all the others. Therefore, the total number of variables is $(5N_p/2 - 1)$.

As a part of the optimization, a series of constraints were enforced. In particular, the propellers must not overlap, their centre must be within the wing's total aperture, the rotational speed $n_{p,i}$ must be limited to avoid falling into a transonic condition, and the thrust of each propeller must be positive, given that this is the logical scope of a propulsion system in cruise flight. If these conditions are not satisfied, a penalty score is assigned as output of the optimization function. Instead, if the constraints are respected, the numerical framework then computes the wake characteristics for each propeller using the implemented BEMT and then evaluates the loading distribution using the VLM lifting line wing model.

To maintain a constant total thrust for each configuration, the thrust ($T_{p,i}$) of each $(N/2 - 1)$ propeller was used as an optimization variable. Nevertheless, the propeller thrust is an output given by the BEMT, which instead requires the propeller rotational speed ($n_{p,i}$) as input. To solve this, a look-up table of corresponding n_p and T_p was constructed prior to the optimization, also using the implemented BEMT code. This was done for multiple propeller sizes and pitches to account for the possible variation range of these variables.

The optimization objectives that were chosen are the wing's lift coefficient (C_L), the aerodynamic efficiency (E), and the the global equivalent propulsive efficiency ($\eta_{p,eq}$). This was done at fixed conditions, meaning fixed free stream velocity (V_∞), angle of attack (α) and geometry. The equivalent propulsive efficiency (eq. 1) is defined as the sum of the propeller efficiency ($\eta_{p,i}$) weighted with the power required by each of the N_p propellers.

$$\eta_{p,eq} = \frac{V_\infty \sum_{i=1}^{N_p} T_{p,i}}{\sum_{i=1}^{N_p} (\eta_{p,i}^{-1} T_{p,i} V_\infty)} \quad (1)$$

By this definition, the total power needed to operate the distributed propulsive system $\left(\sum_{i=1}^{N_p} \eta_{p,i}^{-1} T_{p,i} V_\infty \right)$ is equal to the total thrust $\left(\sum_{i=1}^{N_p} T_{p,i} \right)$ multiplied by the velocity (V_∞) divided by the equivalent propulsive efficiency ($\eta_{p,eq}$), giving a unique definition of propulsive efficiency in DEP.

The optimization was performed using the genetic algorithm optimization tool available in the MATLAB suite [37]. With this, an optimization function $f(\mathbf{X})$ (eq. 2) was defined whose outputs are the wing's lift coefficient, the aerodynamic efficiency and the equivalent propulsive efficiency.

$$\begin{cases} f(\mathbf{X}) = [C_L, E, \eta_{p,eq}] \\ \mathbf{X} = [\mathbf{y}_p, \mathbf{R}_p, \mathbf{T}_p, \mathbf{rot}_p, \boldsymbol{\beta}_p] \end{cases} \quad (2)$$

A genetic algorithm approach (e.g [38],[39]) was chosen because it can be applied without having an explicit expression of the optimization function $f(\mathbf{X})$. Other approaches, as gradient descent [40], require an explicit expression of $f(\mathbf{X})$. This is then used to compute the gradient of the optimization function relative to each optimization variable, to then update the current best value for each constituent of \mathbf{X} . Although genetic algorithms do not have this limitation, they are usually slower to converge. This means that more iterations, generations in the context of genetic algorithms, are needed, stressing the need for an optimization function with a low computational cost.

Two different optimization approaches were used: single-objective and multi-objective optimization [41]. The former optimization strategy was used to obtain the configurations that maximized each of the three objectives indicated in eq. 2 independently. Then, with the multi-objective optimization approach, a space of optimal solutions, represented by the Pareto front [42], was found. For this last step, the resulting configurations from the single-objective optimization were included in the initial populations set to the genetic algorithm as a starting point.

macro:

macro:

The optimization outputs were assessed in terms of the relative increment, in percentage, with respect to an isolated wing configuration, namely, $\Delta C_{L,\%}$ and $\Delta E_{\%}$, and defined as for the generic variable χ as,

$$\Delta\chi_{\%} = 100 \frac{\chi - \chi_{iw}}{\chi_{iw}}. \quad (3)$$

where the subscript iw identifies the isolated wing. Although the comparison against a twin propeller configuration would be more appropriate, using the isolated wing as a reference provides a metric that is independent of the propeller configuration and operating conditions of a reference of choice. The developed framework can be downloaded from a dedicated GitHub repository*.

C. Methodology validation

To validate the BEMT solver, experimental results taken from [43] were used, featuring a two-bladed propeller, with a 150 mm diameter, operating in forward flight conditions and at 7000 revolutions per minute (rpm). The blade geometry and experimental setup characteristics are indicated in [43]. The direct comparison is reported in Figure 4, showing that the developed BEMT correctly predicts the performance of the propeller. The relative percentage error

*https://github.com/enricoamico97/FCG_repository/tree/d5770f7705e38120390b0536bacac2dfe7a661cf/Script/Matlab/DEP_Optimization_DEP_VLM

between the experimental measurements and the numerical prediction for a generic variable χ is defined as:

$$err_{\chi, \%} = 100 \frac{|\chi_{num} - \chi_{exp}|}{|\chi_{exp}|}. \quad (4)$$

For the tested conditions, the average relative error with respect to the experimental measurements is 5.17% for Q_c , 4.59% for T_c , and 1.65% for η .

The implemented VLM was compared with the experimental results reported by Veldhuis [44] of the lift distribution over a wing, as a consequence of the interaction with a propeller slipstream. The reference experimental case is comprised of a rectangular wing measuring 640 mm in semi span ($b/2$) and 240 mm in chord (c), based on a NACA64₂A015 airfoil. The propeller is 4-bladed and has a 236 mm diameter; it is positioned at $y/(b/2) = 0.47$. The specific blade distribution can be found in [44]. The comparison was made at 0° and 4° angle of attack and a freestream dynamic pressure of 2500 Pa, corresponding to a Reynolds number based on the chord of $8 \cdot 10^5$. The propeller operates at $J = 0.85$ with a blade twist equal to 25° at 75% of the blade radius. The blade twist and chord radial distribution can be found in [44]. To numerically reproduce the experimental setup, a full wing with a span of 1.28 m was used, while the symmetry, experimentally provided by the wind tunnel's wall, was achieved by including a second counter-rotating propeller positioned at $y/(b/2) = -0.47$. In total, 101 spanwise segments were used to describe the wing, while the propeller blade is divided into 100 elements in the BEMT implementation. Two cases were used for comparison: inboard-up rotation and outboard-up rotation. The results are reported in Figure 5, showing an average relative error of 5.57%, with a minimum of 0.04% and a maximum of 16.74%, in the estimated cC_l with respect to the reported value for the cases at an angle of attack of 4 degrees.

A second comparison (Figure 6) was made with numerical results obtained with OpenVSP [45]. A rectangular wing with a NACA 3214 airfoil was used, as it was deemed representative of an airfoil used for regional transport aircraft. The wing geometry and the free stream conditions are indicated in table 1 and correspond to wind tunnel conditions. Four APC 8x6x3 propellers at an advance ratio $J = 0.78$ were considered. The OpenVSP simulation was conducted

Table 1 Open VSP comparison test conditions

b [m]	AR	α [°]	C_D	V_∞ [m/s]	N_p
3	7.5	2	0.025	30	4

using a VLM approach and corresponds to the average calculated over 11 complete propellers' full rotations. Each revolution is resolved in ten time steps to allow for enough downstream propagation of the propeller's wake. The wing is discretized in span-wise elements of length $R_p/6$ and 16 chord-wise elements. The propeller's blade is resolved with 20 elements in the radial direction and 10 elements in the blade's chord direction. The results are similar, and the lift distribution computed with the developed code captures the effect of each propeller. The $C_{L, iw}$ computed with

OpenVPS is 1.5% larger with respect to the implemented VLM, while for the case with propellers, the developed code estimated a C_L that is 2.5% larger. By using the developed framework, the computation time is significantly lower than for OpenVSP, one second in contrast with the two hours needed for the OpenVSP simulation. It is worth noting that both results were obtained using the same machine.

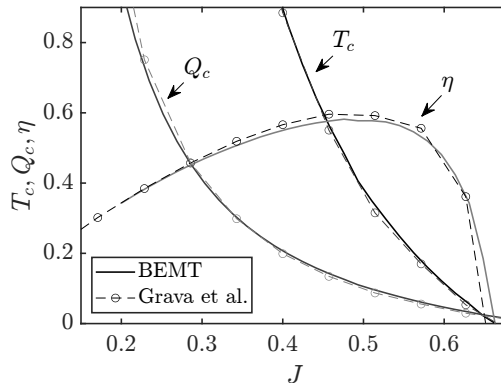


Fig. 4 BEMT results (solid lines) for the thrust coefficient (T_c), the torque coefficient (Q_c) and the efficiency (η) compared with the experimental results (dashed lines) reported in [43].

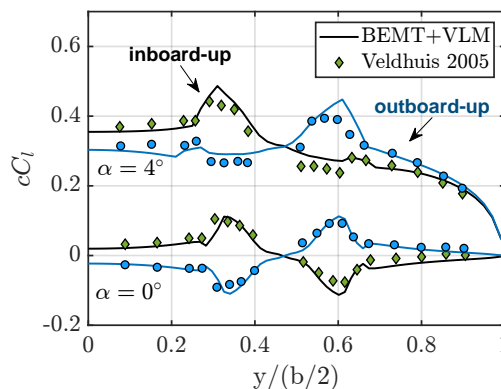


Fig. 5 Lift distribution from the developed numerical model (continuous lines) against the experimental results reported by Veldhuis [44] (diamonds: inboard-up, circles: outboard-up).

III. Case study

The parameters used for the optimization are indicated in table 2. The same airfoil used in section II, a NACA 3214, was selected. The lift coefficient of the isolated wing at the assigned angle of attack is $C_{L,iw} = 0.306$. The propellers are all based on a 5868-9 five-bladed propeller [46], featuring ClarkY wing sections.

Table 2 Fixed parameters of the case study

b [m]	AR	α [°]	C_D	V_∞ [m/s]
24	12	3.5	0.025	100

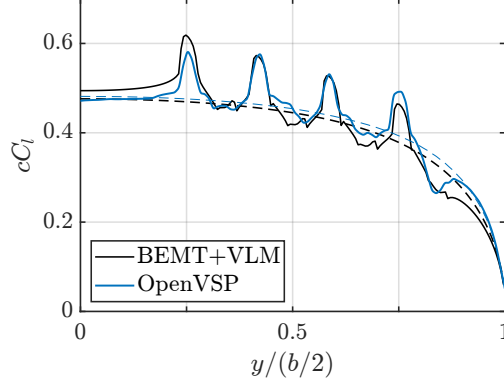


Fig. 6 Aerodynamic load distribution along the wingspan, computed with the developed BEMT+VLM code and with OpenVSP.

We conducted a preliminary exploratory work [47], where all variables were free to change independently and the number of propellers was fixed to four. The results showed a distinction between *inner* and *outer* propellers. The former reached a similar optimal condition, while for the *outer* a different combination of variables was obtained. In addition, the outer propeller was always located at the wing tip as a result of the optimization. Furthermore, the inboard-up rotation direction was deemed optimal in most cases, as it is documented in the literature [48].

The mentioned results were enforced in the present study to minimize the number of optimization variables. All propellers were made inboard-up and *inner* propellers differed only by the spanwise location, but not by geometry, thus making a clear distinction between the $(N_p/2 - 1)$ *inner* propellers and one outboard propeller. This allowed to reduce the total number of variables to $(N_p/2 + 5)$.

Compressibility effects were also taken into account through the use of the Prandtl-Glauert correction [49] when estimating the polars used for the BEMT. The critical Mach number was included in the airfoil polars database. With this, it is possible to evaluate if a given set of operating conditions and design variables leads to a transonic flow, for which the Prandtl-Glauert correction loses validity. To account for this, a last constraint was enforced to the optimizer. In particular, a propeller for which the station at 75% of its radius sees a relative Mach number equal to its critical Mach number was discarded.

A total of six cases were studied, with an increasing number of propellers, namely N_p equal to 2, 4, 6, 8, 10, and 12. For each case, the optimization objectives are C_L , E , and $\eta_{p,eq}$. The discussion will mainly focus on the optimized C_L and E results.

IV. Results

The optimized configurations are plotted in a $\Delta C_{L,\%} - \Delta E_{\%}$ plane, as shown in Figure 7. Each data point belongs to the Pareto front for each respective N_p case. The color coding indicates the global propulsive efficiency ($\eta_{p,eq}$), and the size of the coloured markers corresponds to the equivalent disk loading (from here on indicated as $eqDL$), defined as the

total thrust divided by the total propeller disk surface. It can be seen how configurations with a greater increase in lift (right side of the chart) correspond to a larger disk loading (larger markers) and how the propulsive efficiency is smaller for these configurations. For the optimized $\Delta E_{\%}$ configurations, the disk loading is smaller. Another observation drawn from Figure 7 is that the number of propellers is linked to a larger lift augmentation and larger aerodynamic efficiency.

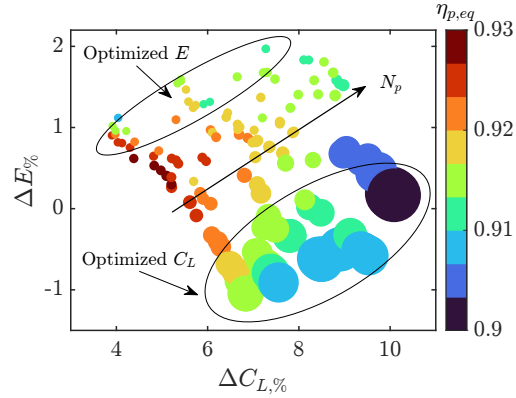


Fig. 7 Optimized configurations: the colour coding corresponds to the equivalent propulsive efficiency $\eta_{p,eq}$ while the disk's dimension indicates the equivalent disk loading ($eqDL$).

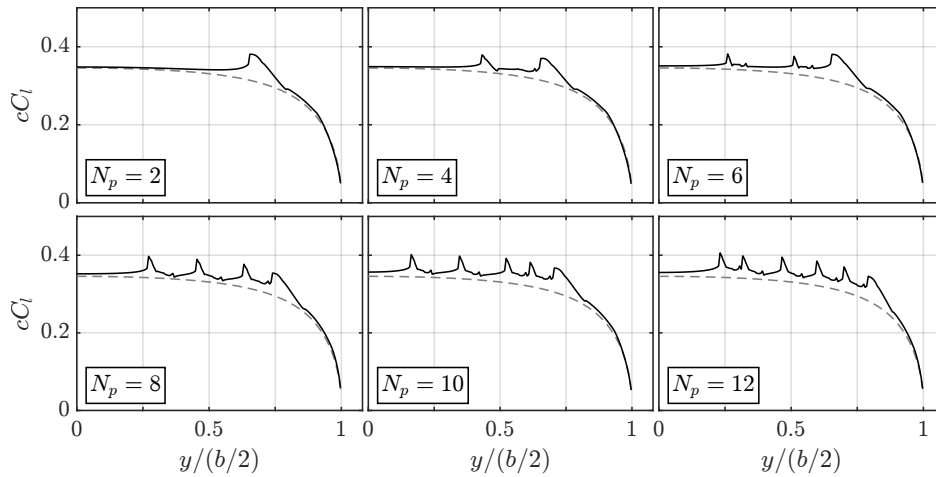


Fig. 8 cC_l distribution for optimized E , cases with N_p equal to 2, 4, 6, 8, 10, and 12.

The resulting spanwise lift distributions are reported in Figures 8 and 9. The plots correspond to cases where the optimization target is the aerodynamic efficiency (Figure 8) or the lift coefficient (Figure 9). It can be seen how the lift distributions, corresponding to the configurations where E is optimized, are closer to the case without propellers. Conversely, the optimized lift cases are generally farther apart from the isolated propeller case, since the lift augmentation is linked with a drag increase and a reduction in aerodynamic efficiency ($\Delta E_{\%} < 0$) for most of the optimized lift cases in Figure 7.

A more quantitative discussion can be made analysing Figures 10. The outboard propeller size, indicated as the ratio between its radius and the wing's chord (R_{out}/c), is larger for the optimized E configurations with respect to

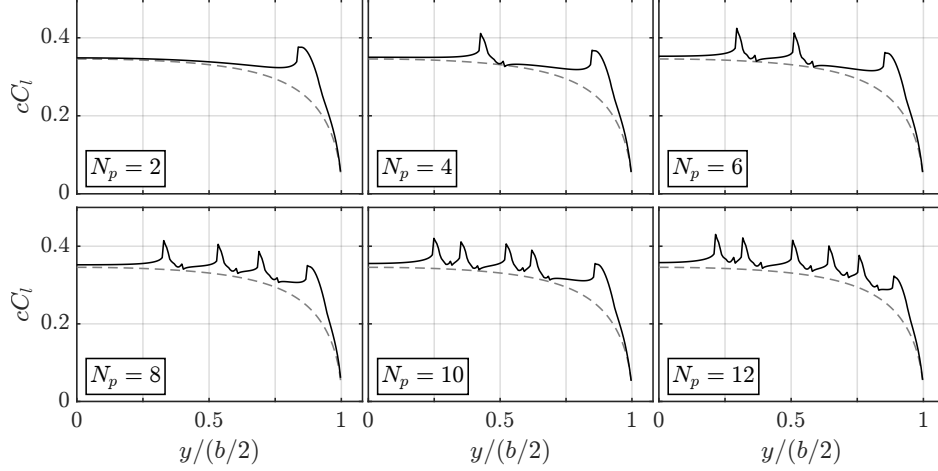


Fig. 9 cC_l distribution for optimized C_L , cases with N_p equal to 2, 4, 6, 8, 10, and 12.

the optimized C_L case. For the latter, however, there is less difference between R_{inn}/c and R_{out}/c . The thrust is distributed towards the wing tip, as it can be inferred from the value of $T_{out}/(T_{tot}/2)$ in Figures 10a and 10c. Large ΔE_{η_0} configurations feature a greater fraction of thrust assigned to the outer propeller with respect to the large $\Delta C_{L,\eta_0}$ configurations. All of the optimized configurations show that, for increasing N_p , the thrust is more evenly distributed among outer and inner propellers. For the optimized C_L case with 12 propellers, 21% of the total thrust is assigned to the outer propeller, which means that each inner propeller is responsible for 5.8% of the total thrust. Conversely, for the 8 propeller optimized C_L case, the outer and each inner propeller are accountable for 35% and 5%, respectively.

Another interesting finding from the results shown in Figure 10 concerns the blade twist (β). The outer tip propeller has a much larger β than the inner propellers, for all configurations. The reason for this is that only the up-going blade side interacts with the wing, and therefore, the effect of the induced upwash behind the UBS is exploited for lift enhancement, which can be appreciated in the lift distributions in Figure 9. For the inner propellers, this cannot be done as the induced downwash from the DBS gives a negative contribution to lift augmentation.

Figure 11 shows the Pearson correlation coefficient (ρ) between the optimization objectives ($\Delta C_{L,\eta_0}$, ΔE_{η_0} , η_p) and relevant configuration parameters. A positive correlation between lift enhancement ($\Delta C_{L,\eta_0}$) and thrust coefficient ($T_{c,out}$ and $T_{c,inn}$) is found, which is also directly linked to the equivalent disk loading. In fact, for the same variables, the correlation with ΔE_{η_0} is negative, pointing to the conclusion that configurations that increase lift do not necessarily increase aerodynamic efficiency. The correlation between the thrust assigned to the outer propeller T_{out} and both $\Delta C_{L,\eta_0}$ and ΔE_{η_0} is negative, suggesting that distributing the propulsion is beneficial; however, the value $\rho(\Delta C_{L,\eta_0}, T_{out}) = -0.79$, suggests that this is more so for the lift increase. The relation between T_c , η_p , $\Delta C_{L,\eta_0}$, and $eqDL$, previously discussed, can also be observed with this approach. The lift enhancement is achieved by operating propellers at a higher disk loading, which corresponds to higher thrust coefficients. However, a propeller that induces a higher speed to the flow is usually less efficient than a propeller that achieves the same thrust by moving a larger mass

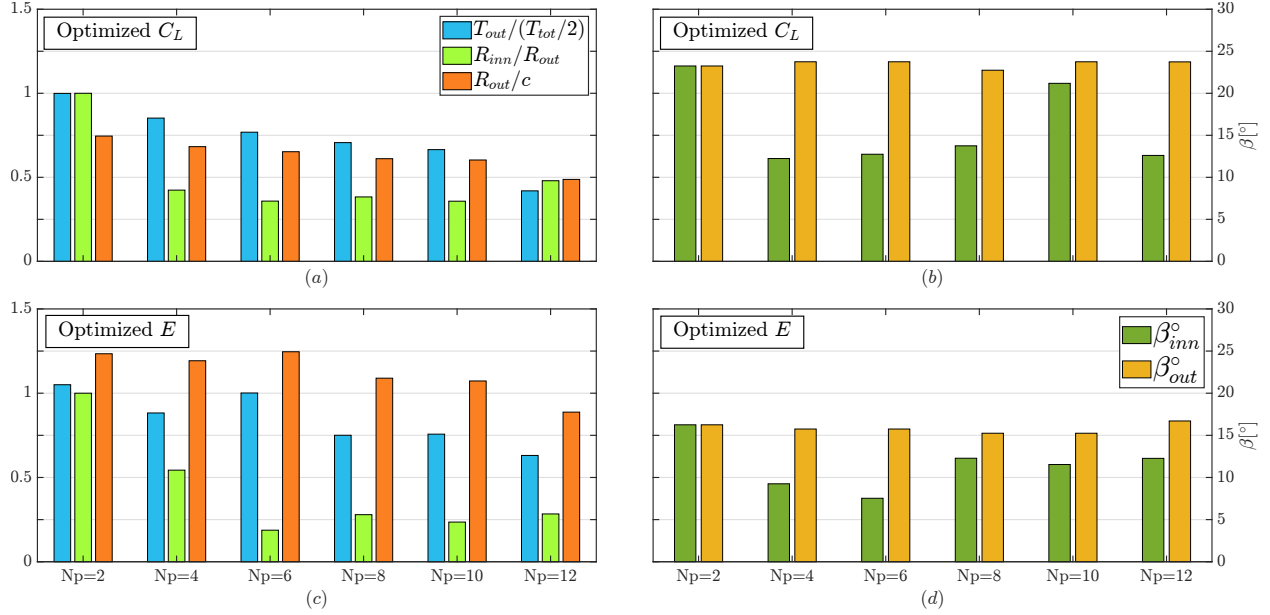


Fig. 10 Distribution of thrust, propeller size, and blade twist among optimized configurations for the C_L optimized configurations: (a) and (b); and for the optimized E cases: (c) and (d).

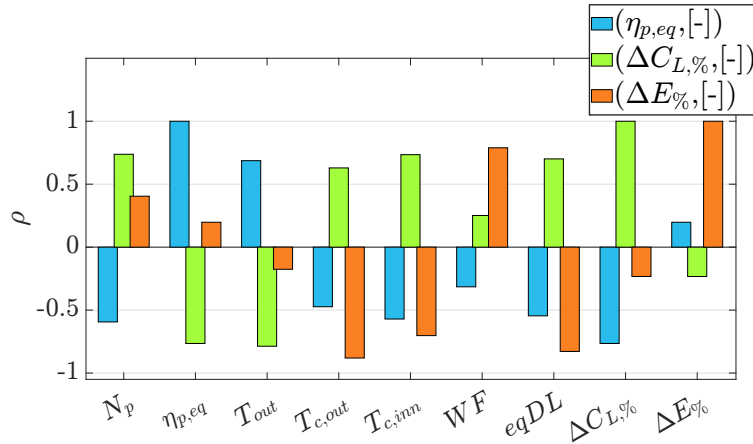


Fig. 11 Pearson's correlation coefficient (ρ) between the optimization objectives ($\Delta C_{L,\%}$, $\Delta E_{\%}$, $\eta_{p,eq}$) and relevant configuration parameters.

flow at a slower speed. All of this explains the negative correlation between lift augmentation and propulsive efficiency. Lastly, there is a strong positive correlation between the washed fraction (WF) and $\Delta E_{\%}$, related to the larger propeller radii, as seen from Figure 10, and to the lower $eqDL$ in Figure 7. WF corresponds to the fraction of the wingspan washed by the slipstream of the propellers, corresponding to the “interaction zone” indicated in Figure 2.

Multidimensional scaling

Multidimensional scaling (MDS) [50] is a dimensionality reduction algorithm that allows to map a multidimensional space to a more interpretable representation, for instance, on two or three dimensions. The optimized solutions found

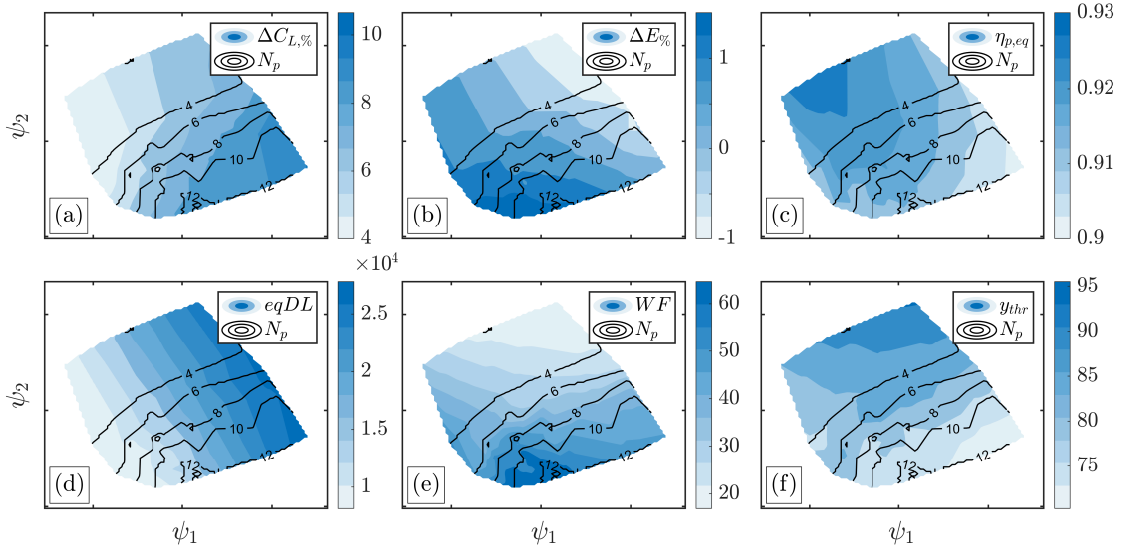


Fig. 12 Maps for (a) $\Delta C_{L,\%}$, (b) $\Delta E_{\%e}$, (c) $\eta_{p,eq}$, (d) equivalent disk loading ($eqDL$), (e) fraction of the wing washed by the propellers slipstream (WF) and (f) thrust center of forces along the semi-span (y_{thr}) in the MDS coordinates (ψ). The isolines represent the number of propellers N_p .

are represented by a series of parameters, such as the optimization objectives ($\Delta C_{L,\%e}$, $\Delta E_{\%e}$, $\eta_{p,eq}$) as well as by the configuration characteristics that allow for those values (e.g. T_p , R_p , among others). Using the MDS algorithm, the level of similarity of the optimized configurations can be evaluated, thus allowing for a lean interpretation of the results. This allows to gain an understanding on how each optimization variable contributes to the optimization objectives. Each configuration is described by the following parameters: N_p , $\Delta C_{L,\%e}$, $\Delta E_{\%e}$, $\eta_{p,eq}$, $\eta_{p,inn}$, $\eta_{p,out}$, $R_{p,inn}$, $R_{p,out}$, $T_{c,inn}$, $T_{c,out}$, WF , $eqDL$, and y_{thr} , defined as the sum of propeller's span-wise position weighted by their respective produced thrust force.

Each of the variables used for describing a configuration can be interpreted as a scalar two-dimensional field described by the coordinates ψ_1 and ψ_2 obtained from the MDS mapping. Figure 12 shows how the optimization relevant parameters are mapped in the MDS coordinates. It is interesting to see how the maximum of each variable is located at different (ψ_1, ψ_2) , showcasing how different objectives require a different mix of parameters. As discussed, the maximum lift augmentation is found at a larger number of propellers as well as for the maximum aerodynamic efficiency. Figures 12a and 12b are different from each other, further indicating that optimizing lift and aerodynamic efficiency might not be achievable simultaneously.

As discussed, a higher lift augmentation is achieved by having a higher disk loading, as it can be deduced from figures 12a and 12d. However, the latter indicates that the number of propellers and the value of the disk loading are uncorrelated, as the isolines are generally perpendicular to each other.

For N_p equal to 12, WF reaches 64% of the wingspan when E is being optimized (Figure 12e). However, when

optimizing the C_L , also for N_p equal to 12, this value is 49%, indicating that larger propellers are associated with greater aerodynamic efficiency. Comparing Figures 12b and Figure 12e it can be inferred that a larger washed fraction is related to a higher aerodynamic efficiency, as the color maps resemble one another, supporting the previous discussion based on the Pearson correlation. The centre of the applied thrust force (y_{thr}) moves inboard for a higher number of propellers (Figure 12f) and in particular for the optimized $\Delta C_{L,\%}$ cases. Nevertheless, the thrust weighted center is placed between 70% and 95% of the semi-span across all optimized DEP configurations, which is still further outboard with respect to the conventional placement at 30-40% in twin turboprop aircraft [44].

V. 3D panel code

As already mentioned, one of the key constraints in the development of the VLM+BEMT model was to keep the computational cost as low as possible. This, however, can come at a cost in terms of accuracy and capability to capture the interaction with non-lifting surfaces. Therefore, we also implemented a 3D panel model. Due to the greater computational time and, as it will be shown, the little differences between this and the VLM+BEMT approach, the 3D panel model was not embedded in the optimization loop.

The effect of the propellers on the wing was included employing a methodology equivalent to the one described in section II, the difference being that in this case the whole propeller disk is considered. The evolution of the propeller slipstream is not modelled, nor is its deformation due to the interaction with the wing.

A comparison between the lifting line method and the panel code approach is shown in Figure 13 for the optimized $\Delta C_{L,\%}$ and $N_p = 8$ case. The percentage relative difference in estimated lift, calculated as the estimated panel code C_L minus the C_L calculated with the lifting line approach, normalized by the latter, is equal to -0.9% , suggesting that both approaches produce comparable spanwise loading distributions.

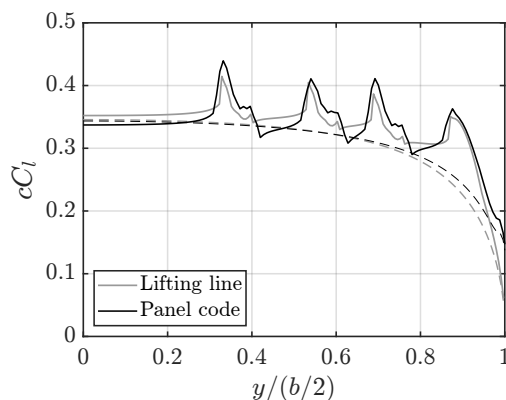


Fig. 13 Comparison between the panel code (black line) and the lifting line method presented in the previous sections (gray line) for the 8-propeller configuration, optimized for maximum lift coefficient.

The greater lift obtained with DEP can have an impact on the stability characteristics, as the wing loading contribution to the pitching moment might increase, as well as the induced downwash to a downstream horizontal tail. To evaluate

this, a comparison is made between the 12 propellers DEP configuration for optimized lift and a reference twin turboprop. The reference configuration has two five-bladed inboard-up rotating propellers with a 3.96 m diameter and, a centre-to-centre distance of 8.1 m. The blade geometry is the same used for the optimization cases. The propeller operating point was chosen to match the total thrust of the DEP configuration while optimizing η_p , resulting in an advance ratio equal to 1.17 and an 86% efficiency. The wing geometry is the same used in section IV. A horizontal tail was added, reproducing a typical configuration of a regional aircraft. The horizontal tail’s airfoil is a NACA 0015 and it is positioned 11.5 m downstream of the wing and 3.8 m above it, in a T-tail configuration. Its geometry is reported in table 3. The plane centre of mass was placed at 40% of the mean aerodynamic chord.

Table 3 Horizontal tail geometry

root chord [m]	tip chord [m]	span [m]
1.76	1	7.3

The trim condition (i.e. null pitching moment calculated with respect to the imposed location of the centre of gravity) was found for both cases by changing the horizontal tail pitch angle.

The pressure coefficient (C_p) distribution over the wing obtained with the panel code is shown for both cases in Figures 14a and 14b. The fuselage is not part of the vortex lattice, and its influence on the flow is neglected. The spanwise lift coefficient distributions for both cases are shown in Figure 15, and the wing’s lift coefficient associated with the considered DEP configuration is 15% higher than the wing’s C_L in the reference case. To obtain a balanced condition for the DEP configuration, the lift produced by the tail had to be increased by 7.3% with respect to the reference configuration.

Although this is a single test case with limited generalizability, these considerations can serve as an example of the impact of DEP for the design of two lifting surfaces configurations.

VI. Conclusions

An optimization framework, based on genetic algorithms, is developed to search for optimal distributed electric propulsion (DEP) configurations based on tractor propellers. The spanwise load distribution and other main aerodynamic performance indicators are estimated with a purposely build fast numerical aeropropulsive model, based on the blade element momentum theory (BEMT) and on the vortex lattice method (VLM). This approach keeps the computational cost low while describing more complex physics than standard approaches purely based on momentum theory, generally employed in the literature.

The goal of a low computational time was successfully achieved, as equivalent results, obtained with the industry standard panel code OpenVSP used for similar purposes, were obtained in a significantly lower time. In addition, both the BEMT and VLM were validated against experimental results found in the literature.

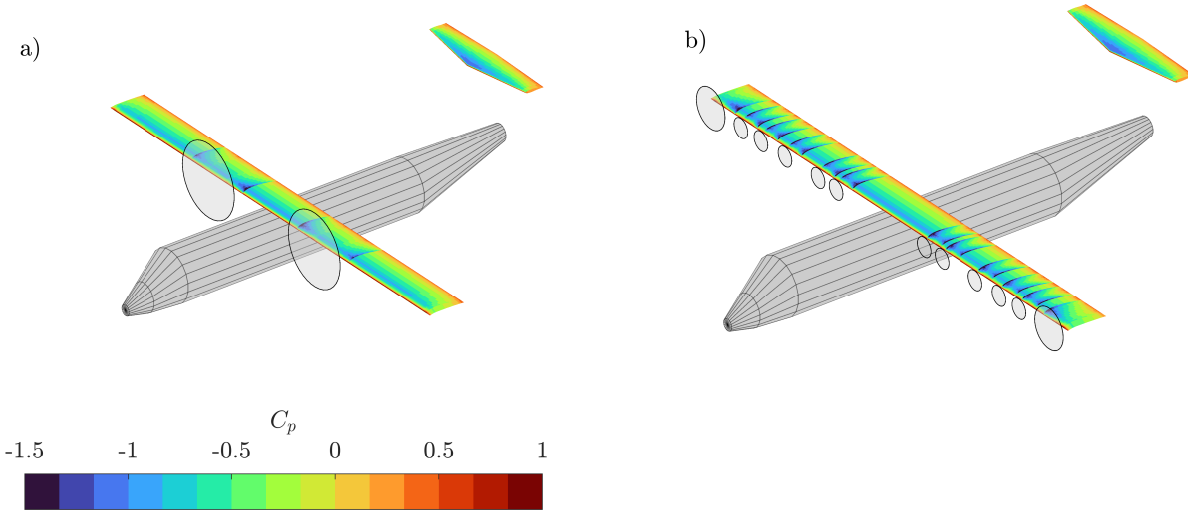


Fig. 14 Contour of the pressure coefficient (C_p) distribution for the twin propeller reference configuration (a) and for the 12-propeller DEP configuration (b), obtained optimizing the lift coefficient.

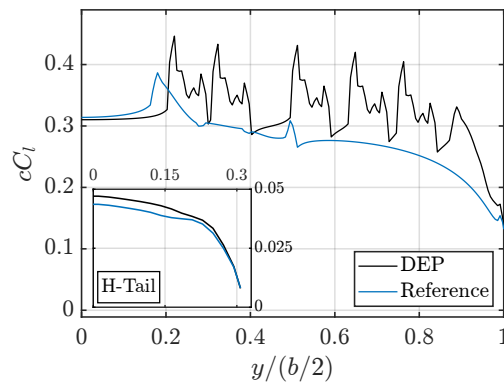


Fig. 15 Comparison between the span-wise lift coefficient distributions on the wing and the horizontal tail. The reference case refers to the twin-propeller configuration. In the insert, the cC_L on the horizontal tail is shown.

A case representative of a regional transport aircraft was analysed, as this aircraft type has been identified as a good target for electric propulsion. Different sets of DEP configurations were found by optimizing the lift coefficient C_L , the aerodynamic efficiency E , and the equivalent propulsive efficiency $\eta_{p,eq}$ through the developed framework. The former two were assessed in terms of the relative increment with respect to an isolated wing configuration, namely: $\Delta C_{L,\%}$, $\Delta E_{\%}$, for which maximum values of 10% and 2% were found.

Across all optimized configurations (from 2 to 12 propellers), a propeller positioned at the wing tip was always found beneficial, in agreement with previous literature. Configurations that optimized E showed outer propellers with greater radii with respect to those that optimized $\Delta C_{L,\%}$. For the latter, a strong correlation was found with the thrust coefficient (T_c) and the equivalent disk loading. However, a negative correlation was found between $\Delta C_{L,\%}$ and the thrust assigned to the outer propeller.

Multidimensional scaling (MDS) proved useful to understand how each optimization variable contributes to the optimization objectives. The configurations that lead to the greatest increase in lift are not the ones that lead to a higher aerodynamic efficiency, indicating that optimizing the C_L and the E might not be achieved simultaneously.

The model itself has some limitations, as discussed in section II. Some aspects as slipstream contraction and propeller-propeller interference, are not included. Some of these limitations could be surpassed by additional corrections to the model as done in [29] for the slipstream evolution. Other limitations instead are peculiar to the chosen numerical model itself (BEMT and VLM), and would require other numerical modelling techniques, for instance VPM (e.g. [21, 51]) for mid-fidelity or other CFD approaches if higher fidelity is required (e.g. [17, 52]). However, the developed numerical framework proved numerically inexpensive, which was an essential requirement to perform multi-parametric optimization.

The presented optimization framework could easily be used for a different optimization objective, or modified to account for other relevant aspects related to power requirements or to the estimated weight, for example. A possible extension could be addressing the sizing and conceptual design, building on the work of De Vries et al. [12], for instance.

Finally, a 3D panel code was implemented, showing a relative difference in the obtained lift coefficient with respect to the BEMT+VLM approach within 0.9%. The implementation of a 3D panel code opens the path towards other studies, focussing for instance on the impact of DEP on the flight stability characteristics of an aircraft, which could also be included in the optimization framework.

Acknowledgments

This study was carried out within the *MOST - Sustainable Mobility National Research Center and received funding from the European Union Next-GenerationEU (PIANO NAZIONALE DI RIPRESA E RESILIENZA (PNRR) - MISSIONE 4 COMPONENTE 2, INVESTIMENTO 1.4 - D.D. 1033 17/06/2022, CN00000023)*. This manuscript reflects only the authors' views and opinions, neither the European Union nor the European Commission can be considered responsible for them.

References

- [1] Baroutaji, A., Wilberforce, T., Ramadan, M., and Olabi, A. G., "Comprehensive investigation on hydrogen and fuel cell technology in the aviation and aerospace sectors," *Renewable and sustainable energy reviews*, Vol. 106, 2019, pp. 31–40. <https://doi.org/10.1016/j.rser.2019.02.022>.
- [2] Alves, P., Silvestre, M., and Gamboa, P., "Aircraft propellers—is there a future?" *Energies*, Vol. 13, No. 16, 2020, p. 4157. <https://doi.org/10.3390/en13164157>.
- [3] Undavalli, V., Olatunde, O. B. G., Boylu, R., Wei, C., Haeker, J., Hamilton, J., and Khandelwal, B., "Recent advancements in

- sustainable aviation fuels,” *Progress in Aerospace Sciences*, Vol. 136, 2023, p. 100876. <https://doi.org/10.1016/j.paerosci.2022.100876>.
- [4] European Union Aviation Safety Agency (EASA), “European Aviation Environmental Report 2025,” Tech. rep., EASA, 2025. URL <https://www.easa.europa.eu/en/domains/environment/eaer>.
- [5] International Civil Aviation Organization (ICAO), “On Board a Sustainable Future: 2016 Environmental Report,” Tech. rep., ICAO, 2016. URL <https://www.icao.int/sites/default/files/sp-files/environmental-protection/Documents/ICAO%20Environmental%20Report%202016.pdf>.
- [6] de Paola, E., Camussi, R., Stoica, L. G., Di Marco, A., and Capobianchi, G., “Aerodynamic and Aeroacoustic Experimental Investigation of a Three Propellers Dep Configuration,” *Available at SSRN 4858399*, 2024. <https://doi.org/10.1016/j.ast.2024.109508>.
- [7] Patterson, M. D., Daskilewicz, M. J., and German, B., “Simplified aerodynamics models to predict the effects of upstream propellers on wing lift,” *53rd AIAA aerospace sciences meeting*, 2015, p. 1673. <https://doi.org/10.2514/6.2015-1673>.
- [8] Chauhan, S. S., and Martins, J. R., “Rans-based aerodynamic shape optimization of a wing considering propeller–wing interaction,” *Journal of Aircraft*, Vol. 58, No. 3, 2021, pp. 497–513. <https://doi.org/10.2514/1.C035991>.
- [9] Schmollgruber, P., Atinault, O., Cafarelli, I., Döll, C., François, C., Hermetz, J., Liaboeuf, R., Paluch, B., and Ridel, M., “Multidisciplinary exploration of DRAGON: an ONERA hybrid electric distributed propulsion concept,” *AIAA Scitech 2019 Forum*, 2019, p. 1585. <https://doi.org/10.2514/6.2019-1585>.
- [10] Deere, K. A., Viken, J. K., Viken, S., Carter, M. B., Wiese, M., and Farr, N., “Computational analysis of a wing designed for the X-57 distributed electric propulsion aircraft,” *AIAA*, 2017, p. 3923. <https://doi.org/10.2514/6.2017-3923>.
- [11] Electra Aero, “Elevating the Future of Air Mobility,” , 2024. URL <https://www.electra.aero>, accessed: 2025-09-09.
- [12] De Vries, R., Brown, M., and Vos, R., “Preliminary sizing method for hybrid-electric distributed-propulsion aircraft,” *Journal of Aircraft*, Vol. 56, No. 6, 2019, pp. 2172–2188. <https://doi.org/10.2514/1.C035388>.
- [13] Massaro, M. C., Biga, R., Kolisnichenko, A., Marocco, P., Monteverde, A. H. A., and Santarelli, M., “Potential and technical challenges of on-board hydrogen storage technologies coupled with fuel cell systems for aircraft electrification,” *Journal of Power Sources*, Vol. 555, 2023, p. 232397. <https://doi.org/10.1016/j.jpowsour.2022.232397>.
- [14] Cardone, L., Petrone, G., De Rosa, S., Franco, F., and Greco, C., “Review of the recent developments about the hybrid propelled aircraft,” *Aerotecnica Missili & Spazio*, Vol. 103, No. 1, 2024, pp. 17–37. <https://doi.org/10.1007/s42496-023-00173-6>.
- [15] Rendón, M. A., Sánchez R, C. D., Gallo M, J., and Anzai, A. H., “Aircraft hybrid-electric propulsion: Development trends, challenges and opportunities,” *Journal of Control, Automation and Electrical Systems*, Vol. 32, No. 5, 2021, pp. 1244–1268. <https://doi.org/10.1007/s40313-021-00740-x>.

- [16] Moore, M. D., “Misconceptions of electric aircraft and their emerging aviation markets,” *52nd Aerospace Sciences Meeting*, 2014, p. 0535. <https://doi.org/10.2514/6.2014-0535>.
- [17] Ribeiro, A. F., Duivenvoorden, R., and Martins, D., “High-Fidelity Simulations of Propeller-Wing Interactions in High-Lift Conditions,” *AIAA AVIATION 2023 Forum*, 2023, p. 3541. <https://doi.org/10.2514/6.2023-3541>.
- [18] Keller, D., “Towards higher aerodynamic efficiency of propeller-driven aircraft with distributed propulsion,” *CEAS Aeronautical Journal*, Vol. 12, No. 4, 2021, pp. 777–791. <https://doi.org/10.1007/s13272-021-00535-5>.
- [19] Niro, C., Savino, A., Cocco, A., and Zanotti, A., “Mid-fidelity numerical approach for the investigation of wing-propeller aerodynamic interaction,” *Aerospace Science and Technology*, Vol. 146, 2024, p. 108950. <https://doi.org/10.1016/j.ast.2024.108950>.
- [20] Savino, A., and Zanotti, A., “Aerodynamic interaction between wing and propeller in eVTOL airplane mode flight condition,” *CEAS Aeronautical Journal*, 2025, pp. 1–14. <https://doi.org/10.1007/s13272-025-00871-w>.
- [21] Alvarez, E. J., and Ning, A., “High-fidelity modeling of multirotor aerodynamic interactions for aircraft design,” *AIAA Journal*, Vol. 58, No. 10, 2020, pp. 4385–4400. <https://doi.org/10.2514/1.J059178>.
- [22] Cole, J. A., Maughmer, M. D., Kinzel, M., and Bramesfeld, G., “Higher-order free-wake method for propeller–wing systems,” *Journal of Aircraft*, Vol. 56, No. 1, 2019, pp. 150–165. <https://doi.org/10.2514/1.C034720>.
- [23] Shen, Y., Wang, Z., Wang, K., Zhou, Z., and Zou, X., “Propulsion/Aerodynamic Coupling Analytic Modeling of Distributed Propulsion Wing Unit with Induced Wing,” *Aerospace Science and Technology*, 2025, p. 110883. <https://doi.org/10.1016/j.ast.2025.110883>.
- [24] Patterson, M. D., Derlaga, J. M., and Borer, N. K., “High-lift propeller system configuration selection for NASA’s SCEPTOR distributed electric propulsion flight demonstrator,” *16th AIAA aviation technology, integration, and operations conference*, 2016, p. 3922. <https://doi.org/10.2514/6.2016-3922>.
- [25] Lee, D., Lim, D., and Yee, K., “Generic design methodology for vertical takeoff and landing aircraft with hybrid-electric propulsion,” *Journal of Aircraft*, Vol. 59, No. 2, 2022, pp. 278–292. <https://doi.org/10.2514/1.C036214>.
- [26] Chakraborty, I., and Mishra, A. A., “Sizing of tilt-wing aircraft with all-electric and hybrid-electric propulsion,” *Journal of Aircraft*, Vol. 60, No. 1, 2023, pp. 245–264. <https://doi.org/10.2514/1.C036813>.
- [27] He, C., Jia, Y., and Ma, D., “Optimization and analysis of hybrid electric system for distributed propulsion tilt-wing UAV,” *IEEE Access*, Vol. 8, 2020, pp. 224654–224667. <https://doi.org/10.1109/ACCESS.2020.3044449>.
- [28] Chauhan, S. S., and Martins, J. R., “Tilt-wing eVTOL takeoff trajectory optimization,” *Journal of aircraft*, Vol. 57, No. 1, 2020, pp. 93–112. <https://doi.org/10.2514/1.C035476>.
- [29] Nederlof, R., Goyal, J., Sinnige, T., Ragni, D., and Veldhuis, L. L., “Fast Numerical Modeling of Propeller–Wing Aerodynamic Interactions,” *AIAA Journal*, 2025, pp. 1–21. <https://doi.org/10.2514/1.J064764>.

- [30] Zhou, W., Ning, Z., Li, H., and Hu, H., “An experimental investigation on rotor-to-rotor interactions of small UAV propellers,” *35th AIAA applied aerodynamics conference*, 2017, p. 3744. <https://doi.org/10.2514/6.2017-3744>.
- [31] de Vries, R., van Arnhem, N., Sinnige, T., Vos, R., and Veldhuis, L. L., “Aerodynamic interaction between propellers of a distributed-propulsion system in forward flight,” *Aerospace Science and Technology*, Vol. 118, 2021, p. 107009. <https://doi.org/10.1016/j.ast.2021.107009>.
- [32] Felli, M., “Underlying mechanisms of propeller wake interaction with a wing,” *Journal of Fluid Mechanics*, Vol. 908, 2021, p. A10. <https://doi.org/10.1017/jfm.2020.792>.
- [33] Sinnige, T., De Vries, R., Corte, B. D., Avallone, F., Ragni, D., Eitelberg, G., and Veldhuis, L. L., “Unsteady pylon loading caused by propeller-slipstream impingement for tip-mounted propellers,” *Journal of Aircraft*, Vol. 55, No. 4, 2018, pp. 1605–1618. <https://doi.org/10.2514/1.C034696>.
- [34] Duivenvoorden, R., Suard, N., Sinnige, T., and Veldhuis, L. L., “Experimental investigation of aerodynamic interactions of a wing with deployed fowler flap under influence of a propeller slipstream,” *AIAA AVIATION 2022 Forum*, 2022, p. 3216. <https://doi.org/10.2514/6.2022-3216>.
- [35] Drela, M., “XFOIL: An analysis and design system for low Reynolds number airfoils,” *Low Reynolds Number Aerodynamics: Proceedings of the Conference Notre Dame, Indiana, USA, 5–7 June 1989*, Springer, 1989, pp. 1–12. https://doi.org/10.1007/978-3-642-84010-4_1.
- [36] Trefftz, E., “Ein gegenstück zum ritzschen verfahren,” *Proc. 2nd Int. Cong. Appl. Mech.*, 1926.
- [37] The-MathWorks-Inc., “MATLAB version: 9.13.0 (R2023a), Global Optimization Toolbox,” , 2023. URL <https://www.mathworks.com>.
- [38] Holland, J. H., *Adaptation in natural and artificial systems: an introductory analysis with applications to biology, control, and artificial intelligence*, MIT press, 1992. <https://doi.org/10.7551/mitpress/1090.001.0001>.
- [39] Konak, A., Coit, D. W., and Smith, A. E., “Multi-objective optimization using genetic algorithms: A tutorial,” *Reliability engineering & system safety*, Vol. 91, No. 9, 2006, pp. 992–1007. <https://doi.org/10.1016/j.res.2005.11.018>.
- [40] Ruder, S., “An overview of gradient descent optimization algorithms,” *arXiv preprint arXiv:1609.04747*, 2016. <https://doi.org/10.48550/arXiv.1609.04747>.
- [41] Deb, K., “Multi-objective optimisation using evolutionary algorithms: an introduction,” *Multi-objective evolutionary optimisation for product design and manufacturing*, Springer, 2011, pp. 3–34. https://doi.org/10.1007/978-0-85729-652-8_1.
- [42] Censor, Y., “Pareto optimality in multiobjective problems,” *Applied Mathematics and Optimization*, Vol. 4, No. 1, 1977, pp. 41–59. <https://doi.org/10.1007/BF01442131>.
- [43] Grava, A., Jacopo, S., Gaetano, I., Luis, B., and Gioacchino, C., “Experimental Investigation of a Small Drone Propeller Aerodynamics in Forward Flight,” *AIAA Journal*, 2024, pp. 1–12. <https://doi.org/10.2514/1.J064664>.

- [44] Veldhuis, L. L. M., “Propeller wing aerodynamic interference,” Ph.D. thesis, Delft University of Technology, 2005. URL <https://repository.tudelft.nl/record/uuid:8ffbde9c-b483-40de-90e0-97095202fbc3>.
- [45] NASA, “Open Vehicle Skeeth Pad,” , 2023. <https://openvsp.org>.
- [46] Hartman, E. P., and Biermann, D., “The aerodynamic characteristics of full-scale propellers having 2, 3, and 4 blades of Clark y and RAF 6 airfoil sections,” Tech. rep., 1938. URL <https://ntrs.nasa.gov/citations/19930091715>.
- [47] Comunian, P., Serpieri, J., and Cafiero, G., “A Genetic-Algorithm Based Approach for Optimized Distributed Propulsion,” *AIAA Aviation Forum and Ascend*, 2024, p. 3603. <https://doi.org/10.2514/6.2024-3603>.
- [48] Sinnige, T., van Arnhem, N., Stokkermans, T. C., Eitelberg, G., and Veldhuis, L. L., “Wingtip-mounted propellers: Aerodynamic analysis of interaction effects and comparison with conventional layout,” *Journal of Aircraft*, Vol. 56, No. 1, 2019, pp. 295–312. <https://doi.org/10.2514/1.C034978>.
- [49] Anderson, J. D., *Modern Compressible Flow With Historical Perspective 3rd Ed.*, McGraw Hill, 2003.
- [50] Kruskal, J. B., and Wish, M., *Multidimensional scaling*, 11, Sage, 1978.
- [51] Wei, J., Lu, B., Zha, Z., and Li, Q., “Aerodynamic modeling of a distributed propulsion system with coupling between propellers, wing, and flaps,” *Aerospace Science and Technology*, 2025, p. 110538. <https://doi.org/10.1016/j.ast.2025.110538>.
- [52] Yang, Z., Meinke, M., and Schroeder, W., “Numerical Analysis of Propeller-Airfoil Interaction in a Distributed Propulsion System Using a Hybrid LES and FW-H Approach,” *30th AIAA/CEAS Aeroacoustics Conference (2024)*, 2024, p. 3211. <https://doi.org/10.2514/6.2024-3211>.
- [53] Ning, A., Hayman, G., Damiani, R., and Jonkman, J. M., “Development and validation of a new blade element momentum skewed-wake model within AeroDyn,” *33rd Wind Energy Symposium*, 2015, p. 0215. <https://doi.org/10.2514/6.2015-0215>.
- [54] McCrink, M. H., and Gregory, J. W., “Blade element momentum modeling of low-reynolds electric propulsion systems,” *Journal of Aircraft*, Vol. 54, No. 1, 2017, pp. 163–176. <https://doi.org/10.2514/1.C033622>.
- [55] Prandtl, L., “Applications of modern hydrodynamics to aeronautics,” 1923. URL <https://ntrs.nasa.gov/citations/19930091180>.

A. Blade element momentum theory

Description

Blade Element Momentum Theory (BEMT) is a low order numerical method that allows for good estimates of the performance of propellers requiring low computing time. It considers the blade’s airfoil and the distribution of both twist β and chord c along its radius. The main insight behind BEMT is to consider both momentum conservation and blade element theory. An expression for thrust (T) and torque (Q) is found with both approaches, subsequently, the

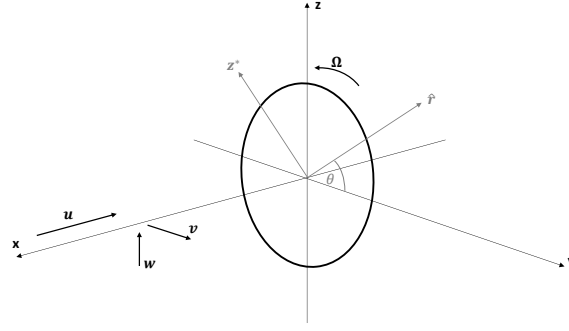


Fig. 16 BEMT reference frame.

expressions obtained from the two formulations are equated. The outputs are the local distribution of forces in the propeller disk, as well as the induced axial velocity and swirl.

A BEMT model capable of considering a non-perpendicular inflow velocity is presented. The main insight behind the numerical model is based on the works [53] and [54]. In Figure 16, the circle represents the propeller disk. u is the main inflow velocity, normal to the propeller plane. v is the inflow velocity along the y axis and w along the z axis.

The elementary thrust dT and torque dQ , corresponding to a small section of propeller disk located at coordinates (r, θ) , can be calculated considering the momentum conservation associated with the elementary mass flow $d\dot{m}$.

$$dT = d\dot{m} (u_w - u_\infty)$$

$$dQ = d\dot{m} v_{t,w}$$

u_w and $v_{t,w}$ are the wake axial and tangential velocities corresponding to a (r, θ) point on the propeller disk. Physically the presence of the propeller produces an increase in the axial velocity behind the propeller disk, as well as an induced swirl velocity. This velocity increment can be described through two parameters a and a' . These are the axial and tangential velocity induction factors at the propeller disk plane.

$$u_d = u_\infty (1 + a)$$

$$v_{t,d} = \Omega r a'$$

The elementary thrust dT and torque dQ corresponding to a (r, θ) point are calculated from momentum conservation (eq. 5 and 6) and from Blade Element Theory (eq. 7 and 8).

Momentum theory

$$dT = 2\rho u_\infty^2 F a (1 + a) r dr d\theta \quad (5)$$

$$dQ = 2\rho u_\infty F a' (1 + a) (\Omega r + v \sin \theta - w \cos \theta) r^2 dr d\theta \quad (6)$$

Blade element theory

$$dT = c_x B \frac{1}{2} \rho W^2 c \frac{r d\theta}{2\pi r} dr \quad (7)$$

$$dQ = c_{z^*} B \frac{1}{2} \rho W^2 c \frac{r d\theta}{2\pi r} dr \quad (8)$$

In equations 5 and 6, F is the Prandtl correction factor for tip losses [55] and ϕ is the angle between the propeller disk plane and the velocity vector \mathbf{W} (Figure 17) seen by the blade.

$$F(r) = \frac{2}{\pi} \cos^{-1} \left[\exp \left(\frac{B(R-r)}{2r|\sin \phi|} \right) \right] \quad (9)$$

In equations 7 and 8 c_x and c_{z^*} are the decomposition of the lift and drag coefficients along the x and z^* directions indicated in Figure 17. By equating equation 5 with 7 and 6 with 8 two equations are found. The term indicated as σ' is the *local solidity*, which corresponds to the ratio between the blade element surface and the corresponding elemental annular surface. It is calculated as the local chord times the number of blades divided by the circumference given by the local radius.

$$a = \frac{1}{\frac{4F \sin^2 \phi}{\sigma' c_x} - 1} \quad (10)$$

$$a' = \frac{1}{\frac{4F \sin \phi \cos \phi}{\sigma' c_{z^*}} + 1} \quad (11)$$

The problem has three unknowns, a , a' , and ϕ . A third equation for ϕ can be found from the definition of $\tan \phi$.

$$\frac{\sin \phi}{\cos \phi} = \frac{u_\infty (1 + a)}{(\Omega r + v \sin \theta - w \cos \theta) (1 - a')} \quad (12)$$

Solution methodology

Given the non linearity of the system of equations described by equations 10, 11 and 12, an iterative procedure must be implemented. This is achieved by defining a residual function $res(\phi)$ obtained by modifying equation 12. The steps

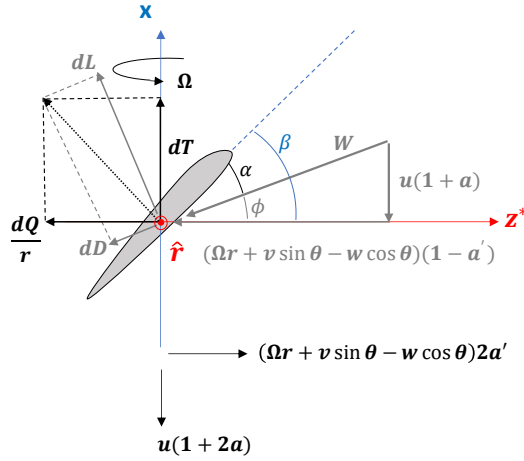


Fig. 17 Forces and velocities in the blade's reference frame.

to follow to compute the residual are then:

$$W = \sqrt{u_{\infty}^2 + (\Omega r + v \sin \theta - w \cos \theta)^2}$$

$$Re = \frac{\rho W c}{\mu}$$

$$\alpha = \beta - \phi$$

$$c_l = c_l(Re, \alpha)$$

$$c_d = c_d(Re, \alpha)$$

$$c_x = c_l \cos \phi - c_d \sin \phi$$

$$c_{z^*} = c_l \sin \phi + c_d \cos \phi$$

$$F = \text{see eq: 9}$$

$$a = \text{see eq: 10}$$

$$a' = \text{see eq: 11}$$

$$res(\phi) = \sin \phi (\Omega r + v \sin \theta - w \cos \theta) \left(\frac{1 - a'}{1 + a} \right) - \cos \phi$$

The lift and drag coefficients (c_l and c_d) are procured from a look-up table of polar curves for the given airfoil, previously obtained with *XFOIL*. The Prandtl-Glauert correction can be applied to the coefficients to include the effects of compressibility.

The solution is found by minimizing $res(\phi)$. After solving the system of equations, the local forces per unit surface at coordinates (r, θ) are calculated according to equations 13 and 14. The total thrust and torque forces can then be

found by integrating the local forces across the entire propeller disk plane. In addition, the in-plane forces can also be evaluated.

$$\delta T(r, \theta) = c_x \rho W^2 \frac{Bc}{4\pi} \quad (13)$$

$$\delta Q(r, \theta) = c_z \rho W^2 \frac{Bc}{4\pi} r \quad (14)$$